UC Berkeley

UC Berkeley Previously Published Works

Title

Mapping Spatiotemporal Solvent Velocity from Measured Concentration Gradients in a Polarized Electrolyte

Permalink

https://escholarship.org/uc/item/49r6z1gt

Journal

Journal of The Electrochemical Society, 172(2)

ISSN

0013-4651

Authors

Abdo, Emily E Patel, Vivaan Mistry, Aashutosh et al.

Publication Date

2025-02-01

DOI

10.1149/1945-7111/adacb0

Copyright Information

This work is made available under the terms of a Creative Commons Attribution License, available at https://creativecommons.org/licenses/by/4.0/

Peer reviewed

Mapping Spatiotemporal Solvent Velocity from Measured Concentration Gradients in a Polarized Electrolyte

Emily E. Abdo, ^{1, 2, #} Vivaan Patel, ^{1,2, #} Aashutosh Mistry, ³ Christopher J. Takacs, ^{4, *} and Nitash P. Balsara ^{1, 2, *}

¹ Department of Chemical and Biomolecular Engineering, University of California, Berkeley, Berkeley, California 94720, USA

² Materials Sciences Division, Lawrence Berkeley National Laboratory, Berkeley, California 94720, USA

³ Department of Mechanical Engineering, Colorado School of Mines, Boulder, Colorado, USA

⁴ SSRL, Materials Science Division, SLAC National Accelerator Laboratory, Menlo Park, California 94025, United States

^{*}These authors contributed equally

^{*} Correspondence to nbalsara@berkeley.edu

Abstract

The electric-field induced motion of neutral species impedes the efficacy of electrochemical devices. By combining *operando* X-ray transmission measurements with continuum mechanics, we have developed a methodology for determining the velocity of neutral solvent molecules under an applied field. The X-ray transmission experiments were used to determine ion concentration profiles as a function of space and time in a polymer electrolyte. The unsteady state solvent mass balance equation was solved numerically with experimental concentration profiles to map spatiotemporal solvent velocities. We compare our experimentally derived results with predictions made with concentrated solution theory. We use the cation transference number as the only adjustable parameter to match experimental measurements of both concentration and solvent velocity. Our approach may be used to determine solvent velocity with any *operando* technique used to measure time-dependent ion concentration profiles.

Introduction

The application of an electric field across an electrochemical cell induces motion within the electrolytic phase. Virtually all electrochemical systems contain binary electrolytes comprising a cation, an anion, and a solvent. In most theoretical papers, the field-induced motion of solvent molecules is ignored. For example, in their classic paper on modeling lithium ion batteries, Doyle, Fuller, and Newman explicitly state that they compute ionic fluxes assuming that the solvent velocity is zero. In a more recent study, Fawdon et al. use the classic solution to the diffusion equation to interpret spatially- and temporally-resolved Raman data obtained from a symmetric cell. Field-induced solvent motion is implicitly ignored in this approach.

At early times, the flux of species i, N_i , is often approximated by:

$$N_i = -z_i u_i F c_i \nabla \phi \tag{1}$$

where z_i , u_i , and c_i denote the charge, mobility, and molar concentration of species i, respectively. $\nabla \phi$ represents the potential gradient, and F is Faraday's constant. In the case of the solvent $z_i = 0$, so it seems reasonable to ignore solvent flux.

In lithium-ion battery applications, a typical electrolyte consists of LiPF₆ salt dissolved in a mixture of ethyl methyl carbonate (EMC) and ethylene carbonate (EC).^{3,4} EMC has a low viscosity and a low dielectric constant, while EC has a high viscosity and a high dielectric constant. It is essential to use a mixture because electrochemical transport is facilitated by a combination of low viscosity and high dielectric constant. Jung et al. studied the field-induced transport of solvent molecules in this mixture and concluded that EC is selectively transported towards the negative electrode.⁵ It appears that the electrolytic phase in a polarized lithium ion battery is extremely viscous at the negative electrode and has a very low dielectric at the positive electrode. There is thus a clear need to improve our understanding of the field-induced motion of solvent molecules.

To our knowledge, there are only two approaches wherein solvent motion is measured explicitly: electrophoretic NMR (eNMR) and *operando* X-ray photon correlation spectroscopy (XPCS). In eNMR, the field-induced solvent velocity is measured by determining phase shift of the NMR spectra. Thus far, this approach is limited to the first instance of polarization when there are no spatial variations in solvent velocity. This technique has not yet been used to map spatiotemporal solvent velocity. In XPCS, which has been used to obtain spatiotemporal data, the solvent velocity is extracted from oscillations in the measured autocorrelation function of the scattered X-rays. 9,10

Our main objective is to show that solvent velocity can be determined directly from spatiotemporal measurements of ion concentrations under applied fields.

Methods

Operando cell measurement:

The details of the electrolyte preparation and assembly for the cell used in this study are described in references 11 and 12 . Briefly, an electrolyte was prepared with SEO(5.1-12.8), a block copolymer containing a 5.1 kg/mol block of polystyrene (PS) and a 12.8 kg/mol block of poly(ethylene oxide) (PEO). SEO(5.1-12.8) was mixed gravimetrically with LiTFSI to achieve a salt concentration of r = 0.04, where r denotes the ratio of lithium ions to ether oxygens. The SEO/LiTFSI electrolyte was then placed in a custom PEEK cell with lithium metal electrodes.

The cell, sealed under an inert environment, was brought to beamline 1-5 at the Stanford Synchrotron Radiation Lightsource (SSRL) and mounted onto a custom heated stage connected to a BioLogic potentiostat. All measurements were conducted at 90 °C, above the melting point of the PEO block. The cell was polarized under a constant current density of i = 0.058 mA/cm² during the X-ray transmission measurements. At each time point, the stage was moved in 100 μ m increments from one electrode to the other to collect spatial transmission information (x direction). The overall thickness of the electrolyte, from one electrode to the other, was L = 2.08 mm. Spatial measurements were normalized such that x/L is bound between 0 at the stripping electrode and 1 at the plating electrode.

The spatially- and temporally-dependent X-ray transmission measurements were then converted to salt concentration r – the details for this process are outlined in references ¹¹ and ¹². The solvent concentration (c₀) and electrolyte concentration (c) were calculated using the approach in the following section. For clarity, the PEEK cell schematic with the x/L axis is shown in Figure 1.

Governing equations:

Based on concentrated solution theory, the one-dimensional transport equations governing the spatiotemporal evolution of salt concentration in an electrolyte in the presence of ionic current i are: 13,14

$$\frac{\partial c}{\partial t} = \frac{\partial}{\partial x} \left(D \left(1 - \frac{d \ln c_0}{d \ln c} \right) \frac{\partial c}{\partial x} \right) - \frac{i}{F} \frac{\partial t_+^0}{\partial x} - \frac{\partial (c v_0)}{\partial x}$$
 (2)

$$\frac{\partial v_0}{\partial t} = \bar{V} \left(\frac{\partial}{\partial x} \left(D \left(1 - \frac{d \ln c_0}{d \ln c} \right) \frac{\partial c}{\partial x} \right) - \frac{i}{F} \frac{\partial t_+^0}{\partial x} \right)$$
(3)

where D is the salt diffusion coefficient, t_+^0 is the cation transference number with respect to solvent velocity v_0 , and \bar{V} is the partial molar volume of the electrolyte. The temporal evolution of salt concentration, quantified by equation 2, depends on solvent velocity v_0 . We thus need two governing equations to simultaneously determine the spatiotemporal evolution of both c and v_0 .

The origin of our Cartesian reference frame is fixed on the positive electrode as shown in Figure 1. All velocities reported in this study (theoretical and experimental) are measured from this reference frame. For the experimentally-applied current density, the interfacial velocity (v_i) of

the positive electrode in a stationary reference frame is found by relating the applied current to lithium's molar mass (M_{Li}) and density (ρ_{Li}) :

$$v_i = -\frac{M_{Li}i}{z_+ F \rho_{Li}} = -0.08 \text{ nm/s}.$$
 (4)

Strictly speaking, concentrated solution theory applies to a homogeneous electrolyte. However, the electrolyte used in this study is a microphase separated block copolymer comprising polystyrene and poly(ethylene oxide) blocks. Thus, parameters such as salt and solvent concentration need to account for the presence of both blocks. c represents the total moles of solvent and salt per unit volume of the electrolyte. A unit volume of electrolyte contains salt, as well as PS and PEO segments. We obtain c from the density of the electrolyte, ρ . The density of PEO/LiTFSI mixtures (ρ_c) as a function of salt concentration is given by:^{15,16}

$$\rho_c = -2.572r^2 + 2.429r + 1.129 \text{ (g/cm}^3). \tag{5}$$

The molar volume of the conducting PEO/LiTFSI microphase (ν_c) per mol of EO monomers can be calculated from this *r*-dependent density:

$$v_c = \frac{M_{EO} + rM_{LiTFSI}}{\rho_c} \text{ (mol/cm}^3\text{)}.$$
 (6)

The properties of the nonconducting PS block are assumed to be constant, with density $\rho_s = 1.035 \text{ g/cm}^3$ and molar volume $v_s = 100.567 \text{ cm}^3/\text{mol}$. Justification for this approximation is given in reference ¹⁷, where it is shown that the glass transition temperature of the PS block in SEO/LiTFSI electrolytes is identical to that of PS homopolymer. The volume fraction of the conducting microphase is then given by:

$$\phi_c = \frac{\nu_c}{\nu_c + s\nu_s} \tag{7}$$

Here s represents the ratio of styrene monomers to ethylene oxide monomers. For SEO(5.1-12.8), s = 0.169. The overall SEO/LiTFSI density is then given by:

$$\rho = \phi_c \rho_c + (1 - \phi_c) \rho_s \tag{8}$$

The molar salt concentration (c) is given by:

$$c = \frac{\rho}{M_{EO} + sM_S + rM_{LiTFSI}} \,. \tag{9}$$

The "solvent" comprises both PS and PEO segments, and the molar solvent concentration (c_0) is given by:

$$c_0 = \frac{\rho - cM_{LiTFSI}}{M_{EO} + sM_S} \,. \tag{10}$$

The solvent concentration and velocity are also related by a material balance,

$$\frac{\partial c_0}{\partial t} = -\frac{\partial (c_0 v_0)}{\partial x} \ . \tag{11}$$

Integrating this equation yields,

$$c_0(x_1)v_0(x_1) - c_0(0)v_0(0) = -\int_{x=0}^{x=x_1} \frac{\partial c_0}{\partial t} dx.$$
 (12)

Given our moving reference frame fixed at the positive electrode, $v_0 = 0$ at x = 0. By applying this boundary condition, we obtain an expression for the solvent velocity at any location x_1 :

$$v_0(x_1) = -\frac{1}{c_0(x_1)} \int_{x=0}^{x=x_1} \frac{\partial c_0}{\partial t} dx.$$
 (13)

Note that v_0 and c_0 are both functions of x and t. Equation 13 can thus be used to calculate v_0 at any value of x and t.

To summarize our approach for obtaining solvent velocity, we measure c(x, t), determine $c_0(x, t)$ using equation 10, and determine $v_0(x)$ for all times using equation 13. The solvent in our case comprises covalently-linked PS and PEO segments. We expect PEO segments in the solvation shell of the cation to have greater velocities than those outside the solvation shell. $v_0(x)$ represents the average velocity of both types of segments at location x. Segmental velocities may vary on the segmental length scale due to effects such as chain stretching. However, since the segments are covalently linked, the average velocities of both types of segments at a given location on coarse-grained continuum length scales will be identical.

Results

We discuss the effect of applying a current density of i = 0.058 mA/cm² through the SEO/LiTFSI electrolyte with an initial concentration $c_{\text{avg}} = 0.65$ M. The current density was chosen to be close to the theoretically estimated limiting current and thus produce a large concentration gradient across the cell. ^{18,19,11} Figure 2a shows the electrolyte concentration as a function of position and time, measured by *operando* X-ray transmission. Measurements obtained at open circuit prior to polarization as well as the first timepoint just after the imposition of current at t = 0.08 h are shown in the inset. The concentration profile at early times is relatively flat and centered around $c = 0.65 \pm 0.02$ M. As time progresses, salt is depleted in the vicinity of the plating electrode (x/L = 1), and it accumulates in the vicinity of the stripping electrode (x/L = 0). At t = 9.85 h, the concentration reaches 0.89 M at x/L = 0.08, and it reduces to 0.32 M at x/L = 0.89.

Figure 2b shows the solvent concentration, c_0 , as a function of position and time. c_0 is calculated using equation 10 with the measured values of c(x,t) shown in Figure 2a. The initial solvent concentration at t = 0.08 h is $c_0 = 16.00 \pm 0.04$ M. With the passage of time, solvent accumulates in the vicinity of the plating electrode and is depleted in the vicinity of the stripping electrode. The data in Figures 2a and 2b reflect mass balance – the accumulation of salt in a given region must be accompanied by the depletion of solvent.

The $c_0(x, t)$ data in Figure 2b is used to calculate $v_0(x, t)$ using equation 13. In Figure 3a, we show a plot of $c_0(t)$ at x/L = 0.08. The curve through the data represents a fit to the functional form:

$$c_0(t) = A \exp(Bt) + C \tag{14}$$

This functional form was used to fit fourteen out of the seventeen datasets obtained at different values of x/L. In Figure 3b, we show data obtained at x/L = 0.89. All fitting was done using the lmfit package in Python;²⁰ the fitted values of A, B, and C and the associated fit errors for each dataset are given in the Supplemental Information (Table T1 and Figure S1). Data obtained at x/L = 0.44, 0.49, and 0.54 were excluded because $\frac{\partial c_0}{\partial t} \approx 0$ near the center of the cell. While we focus on the first 9.85 h of polarization in the discussion below, we fit all our data through t = 20.50 h to obtain accurate extrapolations to steady-state.

The time derivative of c_0 based on equation 14 is given by:

$$\frac{\partial c_0}{\partial t} = A \cdot B \exp(Bt). \tag{15}$$

The fits shown in Figure 3 thus enable calculation of $\frac{\partial c_0}{\partial t}$ at different locations for all times.

Examples of $\frac{\partial c_0}{\partial t}$ obtained at early and late times are shown in Figure 4. The dashed curves in this figure represent hyperbolic sine fits through the data of the form:

$$\frac{\partial c_0}{\partial t} = A_2 \sinh(x - B_2). \tag{16}$$

Fits and associated errors for all timepoints are provided in the Supplemental Information (Table T2).

The hyperbolic sine fits for $\frac{\partial c_0}{\partial t}(x)$ were used to calculate $v_0(x)$ using equation 13 at each time point. The integral on the right side of equation 13 was evaluated analytically. Details of this calculation and error propagation are outlined in the Supplemental Information. The resultant velocities are shown in Figure 5. At all times, v_0 reaches a maximum in the center of the cell and approaches 0 nm/s near the electrodes, as expected by the boundary condition of no solvent flux at the electrode interfaces. Moreover, the velocity at each position decreases with time. At x/L = 0.49, v_0 nearly halves in magnitude from 1.08 ± 0.04 nm/s at t = 0.08 h to 0.61 ± 0.02 nm/s at t = 9.85 h. We expect v_0 to decay to 0 nm/s when the cell is at steady-state, and c_0 is independent of time.

Theoretical modeling from concentrated solution theory

Our objective is to use concentrated solution theory to predict the spatiotemporal dependence of solvent velocity v_0 . In other words, we want to compare the experimental data in Figure 5 with theoretical predictions. The governing equations 2 and 3 were solved using the following boundary conditions and initial condition, as done in reference 21 :

$$-D\left(1 - \frac{d\ln c_0}{d\ln c}\right)\frac{\partial c}{\partial x} = (1 - t_+^0)\frac{i}{v_+ z_+ F} \text{ at } x = 0$$
 (17)

$$-D\left(1 - \frac{d\ln c_0}{d\ln c}\right)\frac{\partial c}{\partial x} = (1 - t_+^0)\frac{i}{v_+ z_+ F} - v_+ c v_0 \text{ at } x = L$$
 (18)

$$v_0 = 0 \text{ at } x = 0$$
 (19)

$$c(x,t=0) = c_{avg} (20)$$

$$v_0(0 < x < L, t = 0) = \bar{V}(1 - t_+^0) \frac{i}{v_+ z_+ F}$$
 (21)

The solution was obtained using the Coefficient Form PDE module in COMSOL Multiphysics 6.1. The PARDISO general solver was used with a domain mesh consisting of 143 elements. Finer refinement was implemented at the electrode boundaries to achieve stable numerical solutions. Based on the chosen reference frame, the plating boundary (x/L=1) can move due to changes in the electrolyte thickness during polarization. Following the calculations given in reference 21 , we show that the change in normalized electrolyte thickness is less than 0.1% for this system, allowing us to neglect the motion of the plating electrode (see Supplemental Information; Figure S3). A time step of 0.296 h was used. This value is similar to the time steps used in the experimental measurements. We need two transport parameters, D and t_+^0 , to calculate $v_0(x,t)$ using equations 2, 3, and 17-21. These parameters were measured by Galluzzo et al. using electrochemical methods for a series of SEO block copolymers mixed with LiTFSI, including SEO(5.1-12.8). Based on the data in reference 22 , we conclude that at r=0.04, $D=[7\pm1.4] \times 10^{-8}$ cm²/s and $t_+^0=0.17\pm0.06$. Previous experimental calculations for a range of salt concentrations have shown these parameters have significant uncertainty. 15,16,22 Therefore, we perform calculations assuming that D and t_+^0 are independent of salt concentration.

The results thus obtained are shown in Figure 6. In Figure 6a, we plot salt concentration, c, as a function of position at selected times. It is evident that the experimental data are in good agreement with theoretical predictions. In Figure 6b, we plot v_0 as a function of position and time. The deviation between theory and experiment is clearly seen in this figure where the predicted velocities lie outside the 95% confidence interval of the measured data. At early times, we see large deviations between theory and experiment. It should be noted that there is significant uncertainty in the experimentally measured values of v_0 at early times because they are dependent on small differences between c(x,t) and c_{avg} (see Figure 6a). As the differences between c(x,t) and c_{avg} increase (e.g. t=5.11 and 9.84h), the discrepancy between theory and experiment reduces.

The uncertainty in the experimentally measured t_+^0 is significant because it involves combining data obtained from four separate experiments.²³ We thus changed the value of t_+^0 to improve the agreement between theory and experiment. In Figure 7, we compare experimental data with predictions assuming $D=7 \times 10^{-8}$ cm²/s and $t_+^0=0.05$. In Figure 7a, we plot salt concentration, c, as a function of position at selected times. Comparing Figures 6a and 7a, we conclude that changing t_+^0 from 0.17 to 0.05 has little effect on the theoretical predictions of c(x,t). In Figure 7b, we plot v_0 as a function of position and time. Comparing Figures 6b and 7b, we conclude that changing t_+^0 from 0.17 to 0.05 has a significant effect on the theoretical prediction of $v_0(x,t)$. In particular, we obtain quantitative agreement between theory and experiment at t=5.11 and 9.84 h.

Since our calculation of solvent velocity is dependent on the time evolution of the solvent concentration, it is instructive to compare the theoretical predictions for solvent concentration to experimental values. In Figure 8a, we plot the experimental salt concentration, c, as a function of time at x/L = 0.08 and compare these results with theoretical predictions. Changing t_+^0 from 0.17 to 0.05 results in a noticeable increase in salt concentration at long times (t = 20 h). The agreement between theory and experiment is better for $t_+^0 = 0.05$. This value of t_+^0 thus provides a consistent prediction of both salt concentration and solvent velocity. In Figure 8b, we compare the experimental solvent concentration as a function of time at x/L = 0.08 with theoretical predictions. Unlike salt concentration which changes by a factor of two in our time window, the solvent concentration only changes by 7%. In this case, there is little difference between the predictions based on $t_+^0 = 0.17$ and $t_+^0 = 0.05$. The inset in Figure 8a shows the theoretical predictions at very early times. The salt concentration exhibits an early time plateau. The corresponding plateau for solvent concentration is shown in the inset in Figure 8b. Obtaining data in the early time regime will require techniques with better spatiotemporal resolution and higher signal-to-noise ratio.

Relevance to other spatiotemporal concentration measurement techniques

The earliest measurements of time-dependent electrolyte concentrations at a fixed position were reported in 1973 using Raleigh interferometry. ^{24,25} Since then, there has been significant improvement in obtaining such data with the advent of *operando* methods such as Raman, NMR, and X-ray techniques.

Raman spectroscopy has been explored since 1998 to map concentration gradients by tracking vibrations of the anion in polymer/LiTFSI systems.^{26–28} Recently, the Pasta group presented Raman measurements of lithium salts in tetraglyme^{29,30} and in ionic liquids². They also used this approach to study a potassium electrolyte³¹.

There has also been success in magnetic resonance imaging (MRI) to generate *operando* electrolyte concentration maps. These investigations employed the ⁷Li and ¹⁹F NMR signals to determine the concentration of LiPF₆ in carbonate-based electrolytes. ^{32,33} Some experiments also couple the use of pulsed-field gradient NMR to simultaneously measure diffusivities. ^{34,35} The MRI method was recently extended to evaluate highly nonideal super-concentrated 3 M LiPF₆ systems, demonstrating the validity of concentrated solution theory. ³⁶ This is relevant to the present study because we have made extensive use of concentrated solution theory to model our data.

The X-ray transmission technique employed in this work has previously been used to track concentration gradients of PEO and SEO electrolytes with LiTFSI. 9,37,12,10,11 Other X-ray approaches include phase imaging approaches, wherein changes in electrolyte density generate contrast to visualize the concentration gradients. Furthermore, it is possible to map gradients by probing F 1s core levels via scanning transmission X-ray microscopy. 9

Our approach for calculating solvent velocities can be applied to any spatiotemporal concentration dataset discussed in this section.

Conclusion

By combining *operando* X-ray transmission measurements with continuum mechanics, we have developed a methodology for calculating solvent velocities based entirely on measured spatiotemporal salt concentration profiles. The calculation requires knowledge of the electrolyte density as a function of concentration, which must either be measured or estimated. The unsteady state solvent mass balance equation is solved numerically with experimental concentration profiles to map solvent velocities as a function of space and time. XPCS is the only other approach for making such measurements.^{9,10}

We compare our experimentally derived results with predictions made with concentrated solution theory. We use the cation transference number as the only adjustable parameter to match experimental measurements of both concentration and solvent velocity. While we have validated our approach using operando X-ray transmission measurements, it can be used to determine solvent velocity regardless of the methodology employed to measure species concentrations.

Since the efficacy of electrochemical devices depends on the motion of the working ion, any motion of the neutral species under an applied electric field incurs an additional energy cost. The motion of charged species, both cations and anions, in a polarized electrolyte can be studied by several standard electrochemical methods. In fact, most of the literature on transport in polarized electrolytes implicitly focuses on the transport of charged species.¹³ The proposed approach is noteworthy because it enables the study of the motion of neutral species in a polarized electrolyte.

Acknowledgements

This work was primarily supported by the Assistant Secretary for Energy Efficiency and Renewable Energy, Office of Vehicle Technologies, of the U.S. Department of Energy, under Contract DE-AC02-05CH11231 under the Battery Materials Research Program. EEA was supported by the National Science Foundation Graduate Research Fellowship Program under Grant No. DGE 2146752. Any opinions, findings, and conclusions or recommendations expressed in this material are those of the author(s) and do not necessarily reflect the views of the National Science Foundation. *Operando* SAXS and transmission measurements were done at SSRL beamline 1-5. Use of the Stanford Synchrotron Radiation Lightsource, SLAC National Accelerator Laboratory, is supported by the U.S. Department of Energy, Office of Science, Office of Basic Energy Sciences under Contract No. DE-AC02-76SF00515. The computations in COMSOL were carried out through the resources provided by the Molecular Graphics and Computing Facility at UC Berkeley under Grant No. NIH S10OD034382. The authors appreciate discussions with Alex J. King and Alhad Deshpande regarding the use of COMSOL and proper implementation of numerical methods.

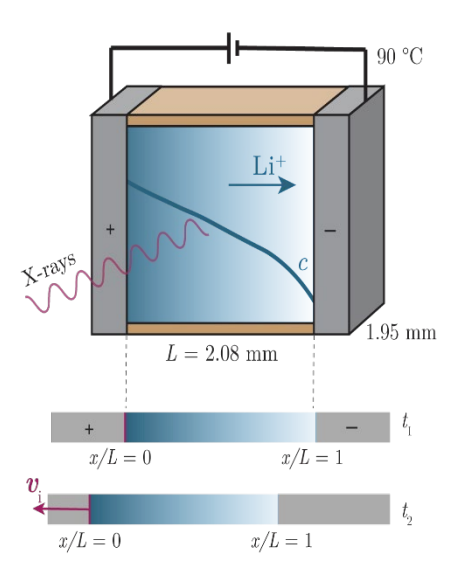


Figure 1. Schematic of *operando* x-ray transmission cell setup. When viewed from a laboratory reference frame, the positive-electrode/electrolyte interface has a constant velocity, v_i , controlled by the applied current. The reference frame used in the theoretical work and analysis of the experimental data is fixed to this interface.

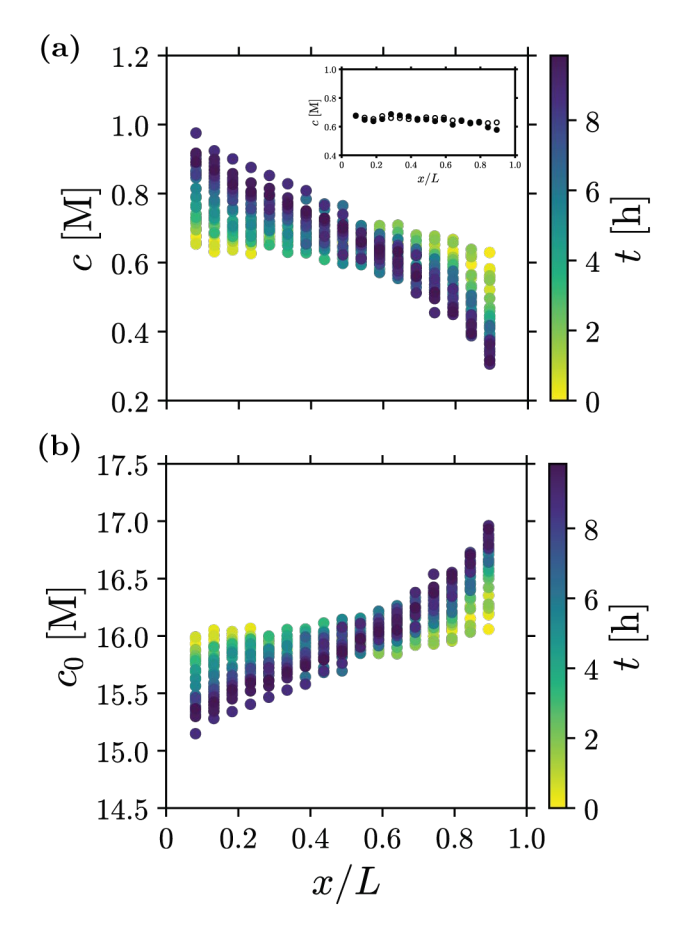


Figure 2. Spatial dependence of the salt (a) and solvent (b) concentration throughout the cell. Color indicates time. The inset in (a) shows the concentration profile at open circuit prior to polarization (open circles) and at the first measurement point at t = 0.08 h (filled circles).

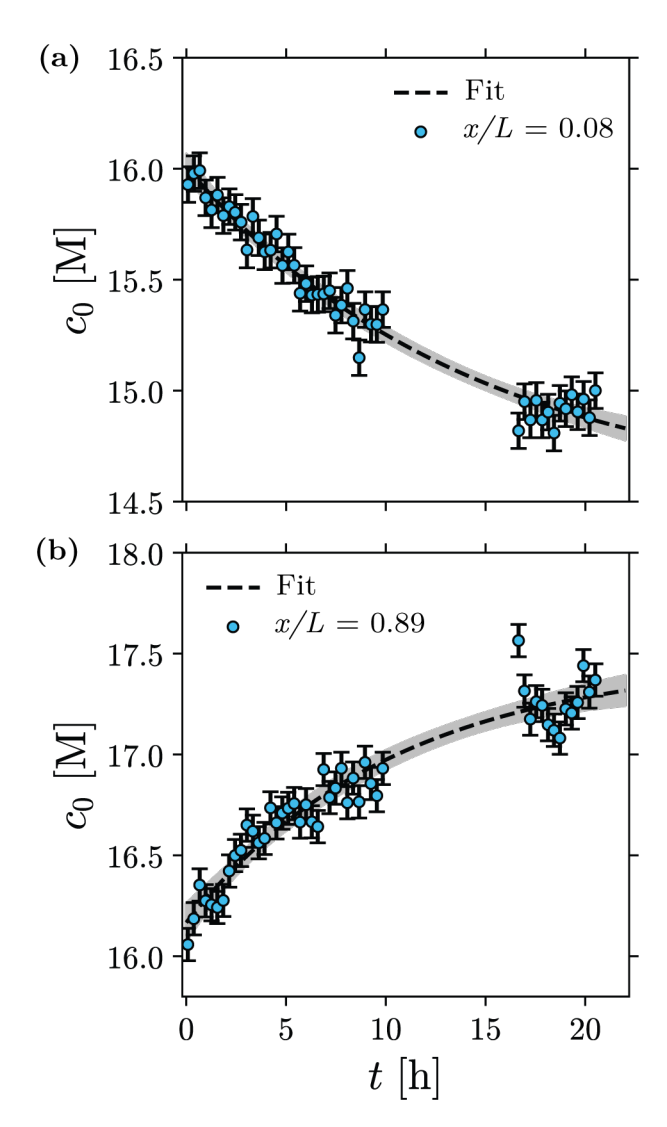


Figure 3. Temporal dependence of the solvent concentration near the stripping electrode (x/L = 0.08) (a) and near the plating electrode (x/L = 0.89) (b). The dashed line shows the exponential fit through the data, and the gray bands represent the 95% confidence interval of the fit. Data was not collected between t = 9.85 and t = 16.65 h due to disruptions in the X-ray beam intensity.

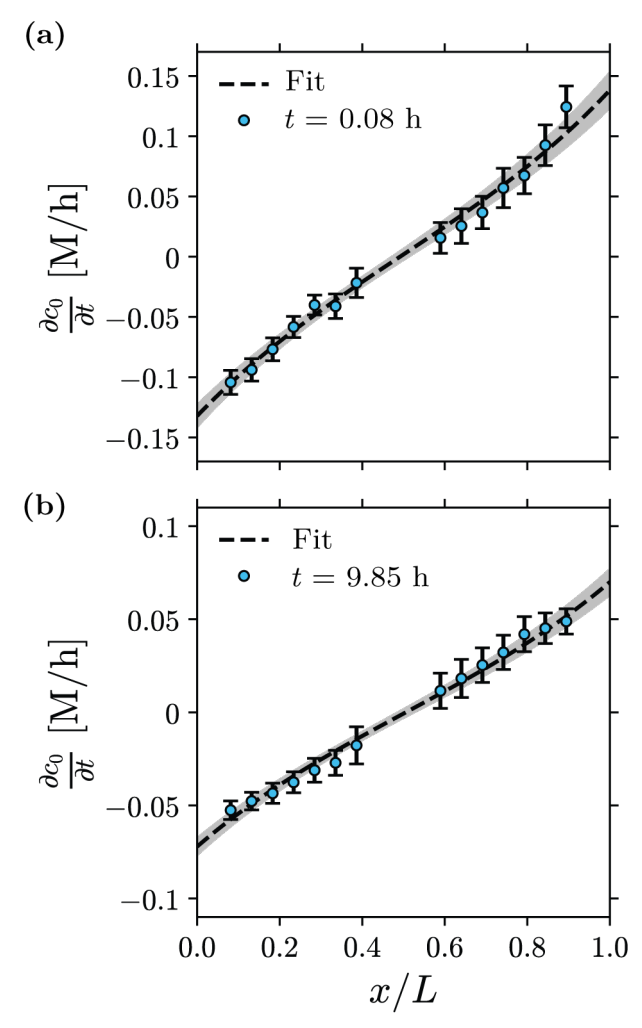


Figure 4. Spatial dependence of the gradient of solvent concentration throughout the cell at t = 0.08 h (a) and t = 9.85 h (b). The dashed line shows the hyperbolic sine fit through the data, and the gray bands represent the 95% confidence interval of the fit. Data obtained between x/L = 0.40 and x/L = 0.55 were excluded from the analysis because changes in the current-induced local concentrations in the middle of the cell were within experimental error, precluding determination of $\partial c_0/\partial t$.

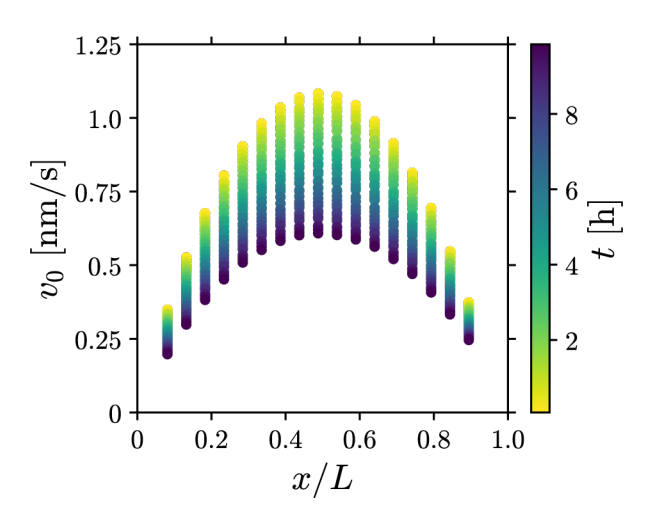


Figure 5. Spatial dependence of the solvent velocity throughout the cell. Color indicates time.

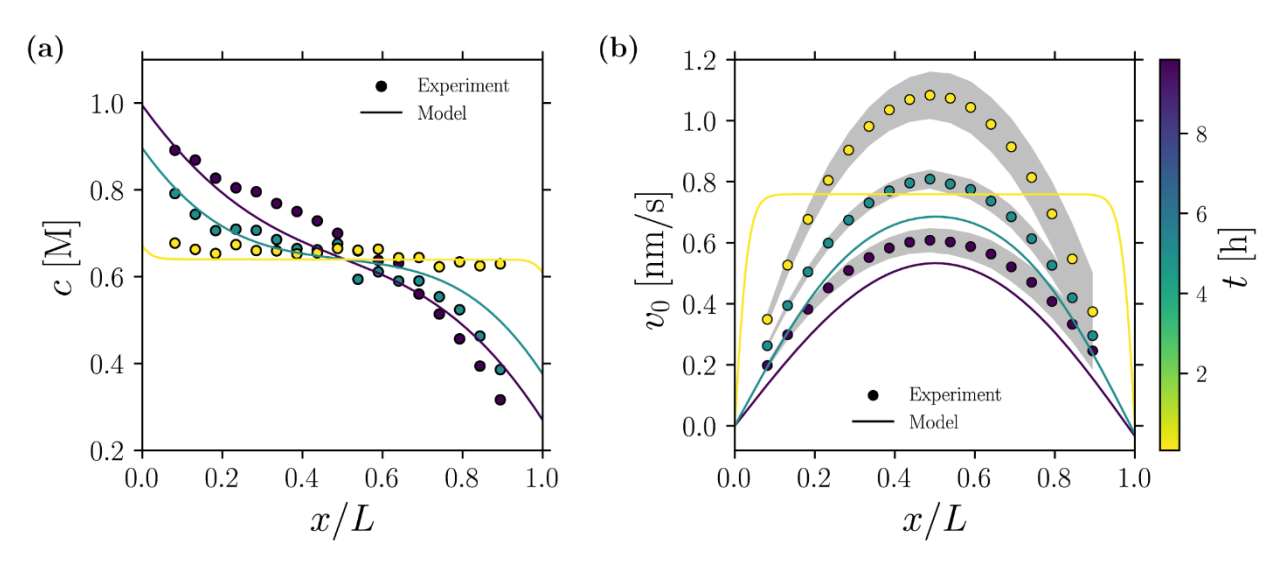


Figure 6. Spatial dependence of salt concentration (a) and solvent velocity (b) for $t_+^0 = 0.17$ and $D = 7 \pm 1.4 \times 10^{-8}$. The grey bands represent 95% confidence intervals for the experimental solvent velocity. Solid lines indicate theoretical predictions. Color bar indicates time. Three time points are shown: t = 0.08 h, t = 5.11 h, and t = 9.84 h.

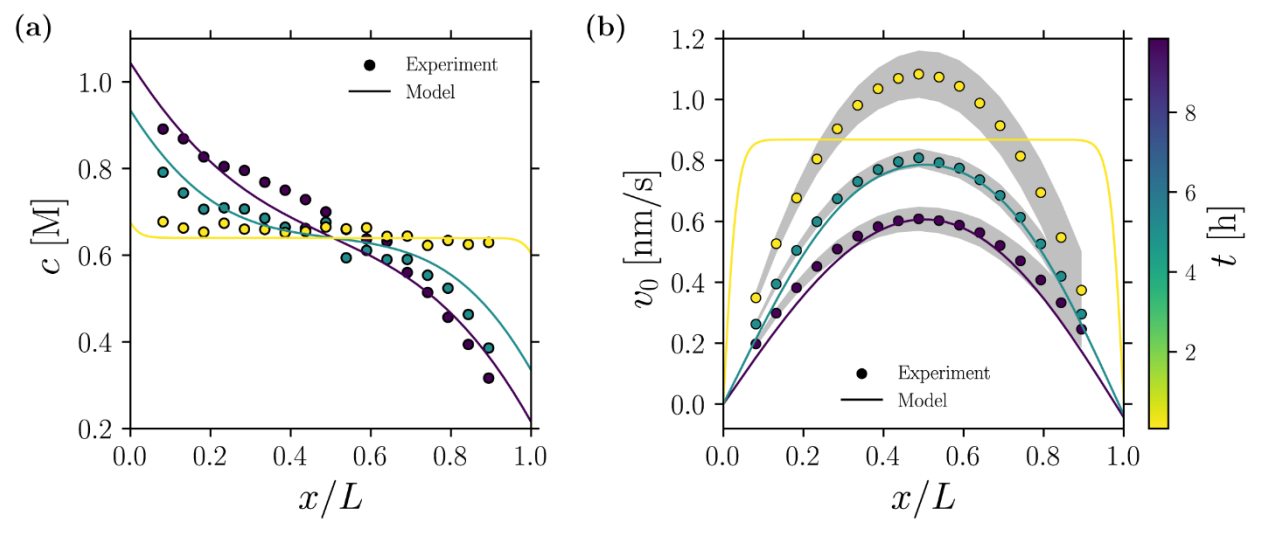


Figure 7. Spatial dependence of salt concentration (a) and solvent velocity (b) for $t_+^0 = 0.05$ and $D = [7 \pm 1.4] \times 10^{-8}$. The grey bands represent 95% confidence intervals for the experimental solvent velocity. Solid lines indicate theoretical predictions. Color bar indicates time. Three time points are shown: t = 0.08 h, t = 5.11 h, and t = 9.84 h.

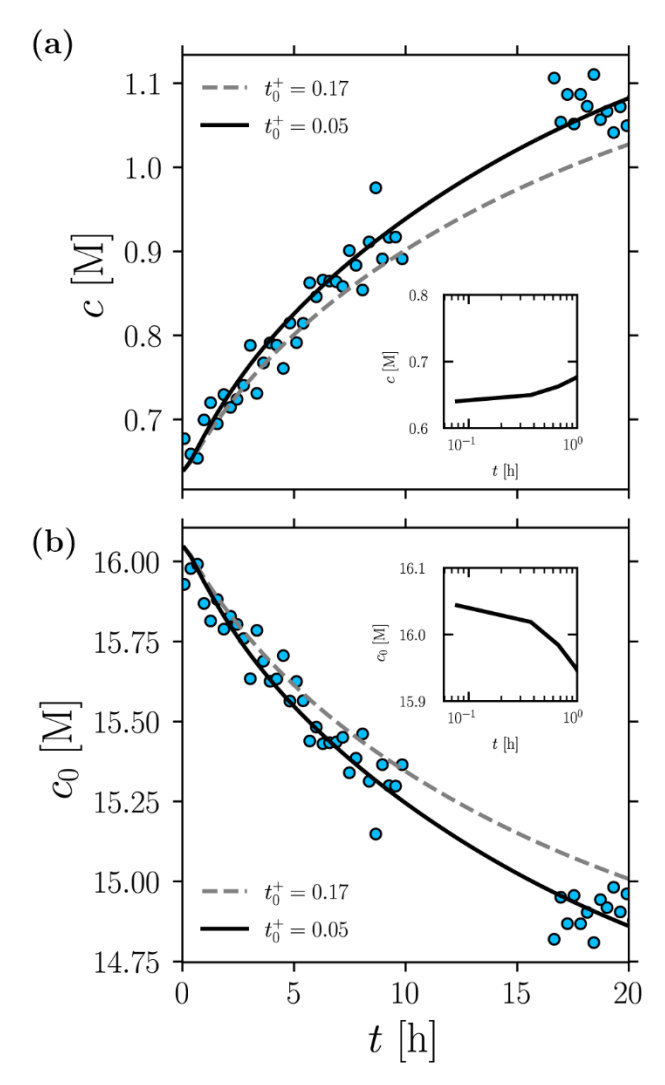


Figure 8. Spatial dependence of salt concentration (a) and solvent velocity (b) near the stripping electrode (x/L = 0.08) shown with blue circles. The theoretical predictions for each concentration assuming $t_+^0 = 0.17$ are shown with a grey dashed line and $t_+^0 = 0.05$ are shown with a solid black line. The insets in (a) and (b) show the salt and concentration values for 0 < t < 1 h on a log scale.

List of Symbols

c Electrolyte concentration (M)

*c*₀ Solvent concentration (M)

D Salt diffusion coefficient (cm^2/s)

F Faraday's constant (96,485 C/mol)

i Current density (mA/cm^2)

L Thickness of electrolyte (electrode-to-electrode distance) (cm)

LiTFSI Lithium bis(trifluoromethanesulfonyl)imide salt

 $M_{\rm EO}$ Molar mass of an ethylene oxide unit (44.05 g/mol)

M_{Li} Molar mass of lithium (6.941 g/mol)

M_{LiTFSI} Molar mass of LiTFSI (287.075 g/mol)

Ms Molar mass of a styrene unit (104.1 g/mol)

 N_i Flux of species $i \text{ (mol/cm}^2/\text{s)}$

PEEK Poly(ether ether ketone)

PEO Poly(ethylene oxide)

PS Polystyrene

Molar ratio of lithium to ether oxygens in the electrolyte ($[Li^+]/[EO]$)

s Molar ratio of styrene to ethylene oxide monomers

SEO Polystyrene-*block*-poly(ethylene oxide)

t Time (h)

 t_{+}^{0} Cation transference number with respect to the solvent

 v_i Velocity of stripping electrode interface (-0.08 nm/s)

 v_0 Solvent velocity (nm/s)

 \overline{V} Partial molar volume of electrolyte (cm³/mol)

x Position in the electrolyte along the direction of ion transport
x/L Position in the electrolyte normalized by the electrolyte thickness

Charge of cation (1 for LiTFSI)

Greek Letters

Stoichiometric coefficient of cation (1 for LiTFSI) ν_{+} Volume of salt-containing conducting phase (nm³/ethylene oxide monomer) u_{c} Volume of styrene phase (0.167 nm³/styrene monomer) $\nu_{\rm s}$ Total density of SEO/LiTFSI electrolyte (g/cm³) ρ Density of salt-containing PEO/LiTFSI conducting phase (g/cm³) ρ_c Density of lithium (0.534 g/cm³) ρ_{Li} Density of polystyrene phase (1.035 g/cm³) ρ_{s} φ Cell potential (V)

Supplemental Information. Details provided on calculating electrolyte density, generating fits for solvent concentration, fitting the time-derivative of solvent concentration, determining solvent velocity at each time point, changes in electrolyte thickness during polarization, and a calibration curve of X-ray transmission and salt concentration.

.

References

- (1) Doyle, M.; Fuller, T. F.; Newman, J. Modeling of Galvanostatic Charge and Discharge of the Lithium/Polymer/Insertion Cell. *J. Electrochem. Soc.* **1993**, *140* (6), 1526–1533. https://doi.org/10.1149/1.2221597.
- (2) Fawdon, J.; Rees, G. J.; La Mantia, F.; Pasta, M. Insights into the Transport and Thermodynamic Properties of a Bis(Fluorosulfonyl)Imide-Based Ionic Liquid Electrolyte for Battery Applications. *J. Phys. Chem. Lett.* **2022**, *13* (7), 1734–1741. https://doi.org/10.1021/acs.jpclett.1c04246.
- (3) Ding, M. S.; Xu, K.; Jow, T. R. Liquid-Solid Phase Diagrams of Binary Carbonates for Lithium Batteries. *J. Electrochem. Soc.* **2000**, *147* (5), 1688. https://doi.org/10.1149/1.1393419.
- (4) Zhang, S. S.; Jow, T. R.; Amine, K.; Henriksen, G. L. LiPF6–EC–EMC Electrolyte for Li-Ion Battery. *J. Power Sources* **2002**, *107* (1), 18–23. https://doi.org/10.1016/S0378-7753(01)00968-5.
- (5) Jung, T.; Wang, A. A.; Monroe, C. W. Overpotential from Cosolvent Imbalance in Battery Electrolytes: LiPF ₆ in EMC:EC. *ACS Omega* **2023**, *8* (23), 21133–21144. https://doi.org/10.1021/acsomega.3c02088.
- (6) Hertz, H. G.; Mills, R. Velocity Correlations in Aqueous Electrolyte Solutions from Diffusion, Conductance and Transference Data. Applications to Concentrated Solutions of 1:2 Electrolytes. *J. Phys. Chem.* **1978**, *82* (8), 952–959. https://doi.org/10.1021/j100497a021.
- (7) Dai, H.; Zawodzinski, T. A. Determination of Lithium Ion Transference Numbers by Electrophoretic Nuclear Magnetic Resonance. *J. Electrochem. Soc.* **1996**, *143* (6), L107–L109. https://doi.org/10.1149/1.1836891.
- (8) Zhang, Z.; Madsen, L. A. Observation of Separate Cation and Anion Electrophoretic Mobilities in Pure Ionic Liquids. *J. Chem. Phys.* **2014**, *140* (8), 084204. https://doi.org/10.1063/1.4865834.
- (9) Steinrück, H.-G.; Takacs, C. J.; Kim, H.-K.; Mackanic, D. G.; Holladay, B.; Cao, C.; Narayanan, S.; Dufresne, E. M.; Chushkin, Y.; Ruta, B.; Zontone, F.; Will, J.; Borodin, O.; Sinha, S. K.; Srinivasan, V.; Toney, M. F. Concentration and Velocity Profiles in a Polymeric Lithium-Ion Battery Electrolyte. *Energy Environ. Sci.* **2020**, *13* (11), 4312–4321. https://doi.org/10.1039/D0EE02193H.
- (10) Galluzzo, M. D.; Steinrück, H.-G.; Takacs, C. J.; Mistry, A.; Grundy, L. S.; Cao, C.; Narayanan, S.; Dufresne, E. M.; Zhang, Q.; Srinivasan, V.; Toney, M. F.; Balsara, N. P. Probing Transference and Field-Induced Polymer Velocity in Block Copolymer Electrolytes. *Cell Rep. Phys. Sci.* **2024**, 101766. https://doi.org/10.1016/j.xcrp.2023.101766.
- (11) Abdo, E. E.; Grundy, L. S.; Galluzzo, M. D.; Loo, W. S.; Fong, A. Y.; Takacs, C. J.; Balsara, N. P. Cylinder-Gyroid Phase Transition in a Block Copolymer Electrolyte Induced by

- Ionic Current. *Macromolecules* **2024**, *57* (2), 503–513. https://doi.org/10.1021/acs.macromol.3c02014.
- (12) Grundy, L. S.; Galluzzo, M. D.; Loo, W. S.; Fong, A. Y.; Balsara, N. P.; Takacs, C. J. Inaccessible Polarization-Induced Phase Transitions in a Block Copolymer Electrolyte: An Unconventional Mechanism for the Limiting Current. *Macromolecules* **2022**, *55* (17), 7637–7649. https://doi.org/10.1021/acs.macromol.2c00922.
- (13) Newman, J.; Balsara, N. P. *Electrochemical Systems*, 4th ed.; Wiley: New York, NY, 2021.
- (14) Balsara, N. P.; Newman, J. Divergence of Velocity Fields in Electrochemical Systems. *J. Electrochem. Soc.* **2022**, *169* (7), 070535. https://doi.org/10.1149/1945-7111/ac8246.
- (15) Pesko, D. M.; Timachova, K.; Bhattacharya, R.; Smith, M. C.; Villaluenga, I.; Newman, J.; Balsara, N. P. Negative Transference Numbers in Poly(Ethylene Oxide)-Based Electrolytes. *J. Electrochem. Soc.* **2017**, *164* (11), E3569–E3575. https://doi.org/10.1149/2.0581711jes.
- (16) Villaluenga, I.; Pesko, D. M.; Timachova, K.; Feng, Z.; Newman, J.; Srinivasan, V.; Balsara, N. P. Negative Stefan-Maxwell Diffusion Coefficients and Complete Electrochemical Transport Characterization of Homopolymer and Block Copolymer Electrolytes. *J. Electrochem. Soc.* **2018**, *165* (11), A2766–A2773. https://doi.org/10.1149/2.0641811jes.
- (17) Yuan, R.; Teran, A. A.; Gurevitch, I.; Mullin, S. A.; Wanakule, N. S.; Balsara, N. P. Ionic Conductivity of Low Molecular Weight Block Copolymer Electrolytes. *Macromolecules* **2013**, *46* (3), 914–921. https://doi.org/10.1021/ma3024552.
- (18) Pesko, D. M.; Feng, Z.; Sawhney, S.; Newman, J.; Srinivasan, V.; Balsara, N. P. Comparing Cycling Characteristics of Symmetric Lithium-Polymer-Lithium Cells with Theoretical Predictions. *J. Electrochem. Soc.* **2018**, *165* (13), A3186–A3194. https://doi.org/10.1149/2.0921813jes.
- (19) Frenck, L.; Veeraraghavan, V. D.; Maslyn, J. A.; Balsara, N. P. Comparing Measurement of Limiting Current in Block Copolymer Electrolytes as a Function of Salt Concentration with Theoretical Predictions. *Electrochimica Acta* **2022**, *409*, 139911. https://doi.org/10.1016/j.electacta.2022.139911.
- (20) Newville, M.; Stensitzki, T.; Allen, D. B.; Rawlik, M.; Ingargiola, A.; Nelson, A. Lmfit: Non-Linear Least-Square Minimization and Curve-Fitting for Python, 2016, ascl:1606.014.
- (21) Mistry, A.; Grundy, L. S.; Halat, D. M.; Newman, J.; Balsara, N. P.; Srinivasan, V. Effect of Solvent Motion on Ion Transport in Electrolytes. *J. Electrochem. Soc.* **2022**, *169* (4), 040524. https://doi.org/10.1149/1945-7111/ac6329.
- (22) Galluzzo, M. D.; Loo, W. S.; Wang, A. A.; Walton, A.; Maslyn, J. A.; Balsara, N. P. Measurement of Three Transport Coefficients and the Thermodynamic Factor in Block Copolymer Electrolytes with Different Morphologies. *J. Phys. Chem. B* **2020**, *124* (5), 921–935. https://doi.org/10.1021/acs.jpcb.9b11066.

- (23) Gao, K. W.; Balsara, N. P. Electrochemical Properties of Poly(Ethylene Oxide) Electrolytes above the Entanglement Threshold. *Solid State Ion.* **2021**, *364*, 115609. https://doi.org/10.1016/j.ssi.2021.115609.
- (24) Newman, J.; Chapman, T. W. Restricted Diffusion in Binary Solutions. *AIChE J.* **1973**, *19* (2), 343–348. https://doi.org/10.1002/aic.690190220.
- (25) Nisancioglu, K.; Newman, J. Diffusion in Aqueous Nitric Acid Solutions. *AIChE J* **1973**, *19*, 797–801. https://doi.org/10.1002/aic.690190417.
- (26) Lassegues, J.-C.; Bruneel, J.-L.; Grondin, J.; Rey, I.; Servant, L.; Vignau, L. Spectroelectrochemistry by Confocal Raman Microspectrometry. *Mol. Cryst. Liq. Cryst. Sci. Technol. Sect. Mol. Cryst. Liq. Cryst.* 1998, 310 (1), 211–218. https://doi.org/10.1080/10587259808045338.
- (27) Rey, I.; Bruneel, J.; Grondin, J.; Servant, L.; Lassègues, J. Raman Spectroelectrochemistry of a Lithium/Polymer Electrolyte Symmetric Cell. *J. Electrochem. Soc.* **1998**, *145* (9), 3034–3042. https://doi.org/10.1149/1.1838759.
- (28) Georén, P.; Adebahr, J.; Jacobsson, P.; Lindbergh, G. Concentration Polarization of a Polymer Electrolyte. *J. Electrochem. Soc.* **2002**, *149* (8), A1015. https://doi.org/10.1149/1.1487832.
- (29) Fawdon, J.; Ihli, J.; Mantia, F. L.; Pasta, M. Characterising Lithium-Ion Electrolytes via Operando Raman Microspectroscopy. *Nat. Commun.* **2021**, *12* (1), 4053. https://doi.org/10.1038/s41467-021-24297-0.
- (30) Olbrich, L. F.; Jagger, B.; Ihli, J.; Pasta, M. Operando Raman Gradient Analysis for Temperature-Dependent Electrolyte Characterization. *ACS Energy Lett.* **2024**, 3636–3642. https://doi.org/10.1021/acsenergylett.4c00954.
- (31) Zhao, J.; Jagger, B.; Olbrich, L. F.; Ihli, J.; Dhir, S.; Zyskin, M.; Ma, X.; Pasta, M. Transport and Thermodynamic Properties of KFSI in TEP by Operando Raman Gradient Analysis. *ACS Energy Lett.* **2024**, *9* (4), 1537–1544. https://doi.org/10.1021/acsenergylett.4c00661.
- (32) Klett, M.; Giesecke, M.; Nyman, A.; Hallberg, F.; Lindström, R. W.; Lindbergh, G.; Furó, I. Quantifying Mass Transport during Polarization in a Li Ion Battery Electrolyte by in Situ ⁷ Li NMR Imaging. *J. Am. Chem. Soc.* **2012**, *134* (36), 14654–14657. https://doi.org/10.1021/ja305461j.
- (33) Chang, H. J.; Ilott, A. J.; Trease, N. M.; Mohammadi, M.; Jerschow, A.; Grey, C. P. Correlating Microstructural Lithium Metal Growth with Electrolyte Salt Depletion in Lithium Batteries Using ⁷ Li MRI. *J. Am. Chem. Soc.* **2015**, *137* (48), 15209–15216. https://doi.org/10.1021/jacs.5b09385.
- (34) Krachkovskiy, S. A.; Bazak, J. D.; Werhun, P.; Balcom, B. J.; Halalay, I. C.; Goward, G. R. Visualization of Steady-State Ionic Concentration Profiles Formed in Electrolytes during Li-

- Ion Battery Operation and Determination of Mass-Transport Properties by *in Situ* Magnetic Resonance Imaging. *J. Am. Chem. Soc.* **2016**, *138* (25), 7992–7999. https://doi.org/10.1021/jacs.6b04226.
- (35) Bazak, J. D.; Allen, J. P.; Krachkovskiy, S. A.; Goward, G. R. Mapping of Lithium-Ion Battery Electrolyte Transport Properties and Limiting Currents with In Situ MRI. *J. Electrochem. Soc.* **2020**, *167* (14), 140518. https://doi.org/10.1149/1945-7111/abc0c9.
- (36) Wang, A. A.; Gunnarsdóttir, A. B.; Fawdon, J.; Pasta, M.; Grey, C. P.; Monroe, C. W. Potentiometric MRI of a Superconcentrated Lithium Electrolyte: Testing the Irreversible Thermodynamics Approach. *ACS Energy Lett.* **2021**, *6* (9), 3086–3095. https://doi.org/10.1021/acsenergylett.1c01213.
- (37) Galluzzo, M. D.; Grundy, L. S.; Takacs, C. J.; Cao, C.; Steinrück, H.-G.; Fu, S.; Rivas Valadez, M. A.; Toney, M. F.; Balsara, N. P. Orientation-Dependent Distortion of Lamellae in a Block Copolymer Electrolyte under DC Polarization. *Macromolecules* **2021**, *54* (17), 7808–7821. https://doi.org/10.1021/acs.macromol.1c01295.
- (38) Takamatsu, D.; Yoneyama, A.; Asari, Y.; Hirano, T. Quantitative Visualization of Salt Concentration Distributions in Lithium-Ion Battery Electrolytes during Battery Operation Using X-Ray Phase Imaging. *J. Am. Chem. Soc.* **2018**, *140* (5), 1608–1611. https://doi.org/10.1021/jacs.7b13357.
- (39) Hudson, W. R. Block Copolymer Electrolytes for Lithium Batteries, UC Berkeley, 2011. ProQuest ID: Hudson berkeley 0028E 11471.